Title

CsV$_3$Sb$_5$: A Z$_2$ Topological Kagome Metal with a Superconducting Ground State

Authors

Ortiz, Brenden R
Teicher, Samuel M.âL.
Hu, Yong
et al.

Peer reviewed

CsV$_3$Sb$_5$: a $\mathbb{Z}_2$ topological kagome metal with a superconducting ground state

Brenden R. Ortiz,[1, *] Samuel M.L. Teicher,[1] Yong Hu,[2] Julia L. Zuo,[1] Paul M. Sarte,[1]
Emily C. Schueller,[1] A.M. Milinda Abeykoon,[3] Matthew J. Krogstad,[4] Stefan Rosenkranz,[4]
Raymond Osborn,[4] Ram Seshadri,[1] Leon Balents,[5] Junfeng He,[2] and Stephen D. Wilson[1, †]

[1]*Materials Department and California Nanosystems Institute,*
University of California Santa Barbara, Santa Barbara, CA, 93106, United States
[2]*Hefei National Laboratory for Physical Sciences at the Microscale,*
Department of Physics and CAS Key Laboratory of Strongly-coupled Quantum Matter Physics,
University of Science and Technology of China, Hefei, Anhui 230026, China
[3]*National Synchrotron Light Source II, Brookhaven National Laboratory, Upton, New York 11973, USA*
[4]*Materials Science Division, Argonne National Laboratory, Argonne, Illinois 60439-4845, USA*
[5]*Kavli Institute for Theoretical Physics, University of California,*
Santa Barbara, Santa Barbara, California 93106, USA
(Dated: November 16, 2020)

Recently discovered alongside its sister compounds KV$_3$Sb$_5$ and RbV$_3$Sb$_5$, CsV$_3$Sb$_5$ crystallizes with an ideal kagome network of vanadium and antimonene layers separated by alkali metal ions. This work presents the electronic properties of CsV$_3$Sb$_5$, demonstrating bulk superconductivity in single crystals with a T$_c$ = 2.5 K. The normal state electronic structure is studied via angle-resolved photoemission spectroscopy (ARPES) and density functional theory (DFT), which categorize CsV$_3$Sb$_5$ as a $\mathbb{Z}_2$ topological metal. Multiple protected Dirac crossings are predicted in close proximity to the Fermi level (E_F), and signatures of normal state correlation effects are also suggested by a high temperature charge density wave-like instability. The implications for the formation of unconventional superconductivity in this material are discussed.

Kagome metals are a rich frontier for the stabilization of novel correlated and topological electronic states. Depending on the degree of electron filling within the kagome lattice, a wide array of instabilities are possible, ranging from bond density wave order [1, 2], charge fractionalization [3, 4], spin liquid states [5], charge density waves [6], and superconductivity [1, 7]. Additionally, the kagome structural motif imparts the possibility of topologically nontrivial electronic structures, where the coexistence of Dirac cones and flatbands promoting strong correlation effects may engender correlated topological states. For instance, the presence of magnetic order [8–10] in kagome compounds has been noted to stabilize novel quantum anomalous Hall behaviors, and electron-electron interactions in certain scenarios are proposed to drive the formation of topological insulating phases [11].

One widely sought electronic instability on a two-dimensional kagome lattice is the formation of a superconducting ground state. Layered kagome metals that superconduct are rare, and the interplay between the nontrivial topology accessible via their electronic band structures and the formation of an intrinsic superconducting state makes this a particularly appealing space for realizing exotic ground states and quasiparticles. Unconventional superconductivity is predicted to emerge via nesting-driven interactions in heavily doped kagome lattices [12]. This mechanism, first pointed out in theories for doped graphene (which shares the hexagonal symmetry of the kagome lattice)[13, 14], relies upon scattering between saddle points of a band at the M points of the 2d Brillouin zone, which are relevant when the system

possesses a nearly hexagonal Fermi surface proximate to a topological transition. Superconductivity potentially competes with a variety of other electronic instabilities at different fillings [11, 15]. Realizing superconductivity in a two-dimensional kagome material that avoids these competing instabilities remains an open challenge.

Recently a new family of layered kagome metals that crystallize in the AV$_3$Sb$_5$ structure (A: K, Rb, Cs) was reported [16]. These materials crystallize into the $P6/mmm$ space group, with a kagome network of vanadium cations coordinated by octahedra of Sb. The compounds are layered, with the kagome sheets separated by layers of the A-site alkali metal ions (Fig. 1). Compounds across the series are high mobility, two-dimensional metals with signatures of correlation effects and potential electronically-driven symmetry breaking. Recent studies have further shown that one variant, KV$_3$Sb$_5$, is a Dirac semimetal with an extraordinarily large anomalous Hall effect in the absence of long-range magnetic order [17]. Remarkably little however remains known about this new class of kagome metals, particularly with regards to their capacity for hosting correlated topological states.

Here we identify that CsV$_3$Sb$_5$, the heaviest member of the new kagome compounds, is a $\mathbb{Z}_2$ topological metal with a superconducting ground state. Angle-resolved photoemission spectroscopy (ARPES) measurements combined with density-functional theory (DFT) calculations reveal the presence of multiple Dirac points near the Fermi level and predict topologically protected surfaces states only 0.05 eV above the Fermi level at the M-points. Furthermore, both ARPES and DFT observe
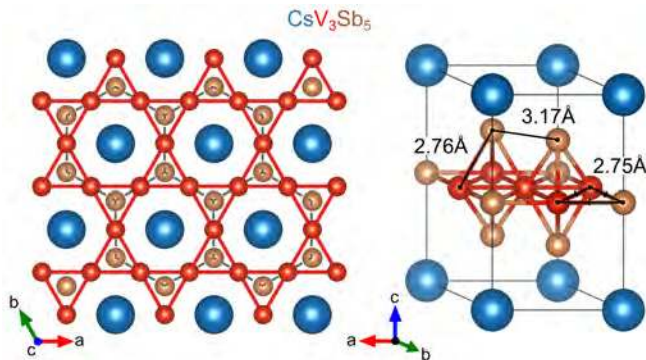
FIG. 1. CsV_3Sb_5 is a layered compound with a structurally perfect kagome network of vanadium. There are two distinct Sb sites in the structure: (1) a simple hexagonal net woven into the kagome layer, and (2) graphite-like layers of antimony (antimonene) above and below the kagome layer. All bonds ≤ 3.2Å have been drawn in the isometric perspective, highlighting the layered nature of CsV_3Sb_5

hexagonal Fermi surfaces, consistent with close proximity of saddle points at M. Magnetization, heat capacity, and electrical resistivity measurements reveal the onset of superconductivity at $T_c = 2.5$ K and further identify a higher temperature $T^* = 94$ K transition suggestive of charge density wave order. Our work establishes CsV_3Sb_5 as a novel exfoliable, kagome metal with a superconducting ground state and protected Dirac crossings close to E_F.

Single crystals of CsV_3Sb_5 were synthesized via a self-flux growth method [18]. Magnetization measurements were performed using a Quantum Design SQUID Magnetometer (MPMS3) in vibrating-sample measurement mode (VSM), and resistivity and heat capacity measurements were performed using a Quantum Design Dynacool Physical Properties Measurement System (PPMS). Angle-resolved photoemission (ARPES) measurements were obtained at the Stanford Synchrotron Radiation Lightsource (SSRL, beamline 5-2), a division of the SLAC National Accelerator Laboratory using 120 eV photons with an energy resolution better than 20 meV. Temperature-dependent X-ray diffraction data was collected at Brookhaven National Laboratory (beamline 28-ID-1) and at the Advanced Photon Source at Argonne National Laboratory (Sector 6-ID-D). Rietveld refinements of temperature-dependent diffraction were performed using TOPAS Academic V6.[19] Structure visualization was performed with the VESTA software package [20], and the electronic structure of CsV_3Sb_5 was calculated in VASP $v5.4.4$ [21–23] using projector-augmented wave (PAW) potentials [24, 25] with details described in the supplemental materials [18].

For an intuitive understanding of the CsV_3Sb_5 structure, we first consider the constituent sublattices. The hallmark two-dimensional kagome network is formed by

the V1 sublattice, and is interpenetrated by a simple hexagonal net of Sb1 antimony. All interatomic distances within the kagome layer are equal (2.75Å), as required by the high symmetry of the V1 (Wyckoff $3g$) and Sb1 (Wyckoff $1b$) sites. The Sb2 sublattice creates graphite-like layers of Sb (antimonene) that encapsulate the kagome sheets. The Cs1 sublattice naturally fills the space between the graphite-like sheets, and the nearest Cs-Sb distance is nearly 4Å.

Bulk electronic properties of CsV_3Sb_5 were studied via electron transport, magnetization, and heat capacity measurements. Figures 2(a, b, c) show characterization data collected across a broad range of temperatures. Magnetization data collected under $\mu_0 H = 1$ T are plotted as susceptibility $\chi = \frac{M}{H}$ in Fig. 2 (a) and show a high temperature response ($T > 100$ K) consistent with Pauli paramagnetism. As a rough estimate, DFT calculations of the density of states at the Fermi level $g(E_F) \approx 10 \, \text{eV}^{-1}\text{cell}^{-1}$ estimate $\chi \approx 200 \times 10^{-6} \, \text{emu} \, \text{Oe}^{-1}\text{mol}^{-1}$, which agrees reasonably well with the experimental data.

At temperatures below 94 K, a sharp drop in the magnetization data denotes the onset of a phase transition, noted as T^*. This transition also appears as an inflection point in the resistivity data shown in Figure 2(b), where temperature-dependent resistivity data with current flowing both in the kagome planes ($\rho_a b$) and between the planes (ρ_c) are plotted. The out-of-plane resistivity is nearly 600 times larger than in-plane, emphasizing the two-dimensional nature of the Fermi surface. Heat capacity data plotted in Fig. 2 (c) also illustrate a strong entropy anomaly at $T^* = 94$ K. The integrated entropy released through the T^* transition is approximately $\Delta S = 1.6 \, \text{J} \, \text{mol}^{-1}\text{K}^{-1}$, and is naively too small to account for collective spin freezing of free V-moments. Instead, it likely arises from freezing within the charge sector [11], suggesting a potential charge/bond density wave anomaly that will be discussed later in this manuscript.

Figures 2(d-f) show the onset of superconductivity in magnetization, resistivity, and heat capacity, respectively. In all cases, the onset of superconductivity occurs at approximately $T_c = 2.5$ K. Magnetization data reveal bulk superconductivity and a well-defined Meissner state, and heat capacity measurements show a sharp entropy anomaly at the superconducting transition, although, due to a limited temperature regime, we are unable to fully characterize the gapped behavior far below T_c. The slight offset in the onset of T_c in electrical resistivity (Figure 2(e)) measurements is due to the high probe currents (8 mA) used in the DC measurement. Reduced currents show T_c return to nominal values, although the data quality suffers significantly due to the low resistivity of CsV_3Sb_5 single crystals.

Having determined that CsV_3Sb_5 is a bulk kagome superconductor with a transition temperature $T_c = 2.5$ K, we next examine the normal state metal via a combination of ARPES measurements and DFT modeling. Fig-
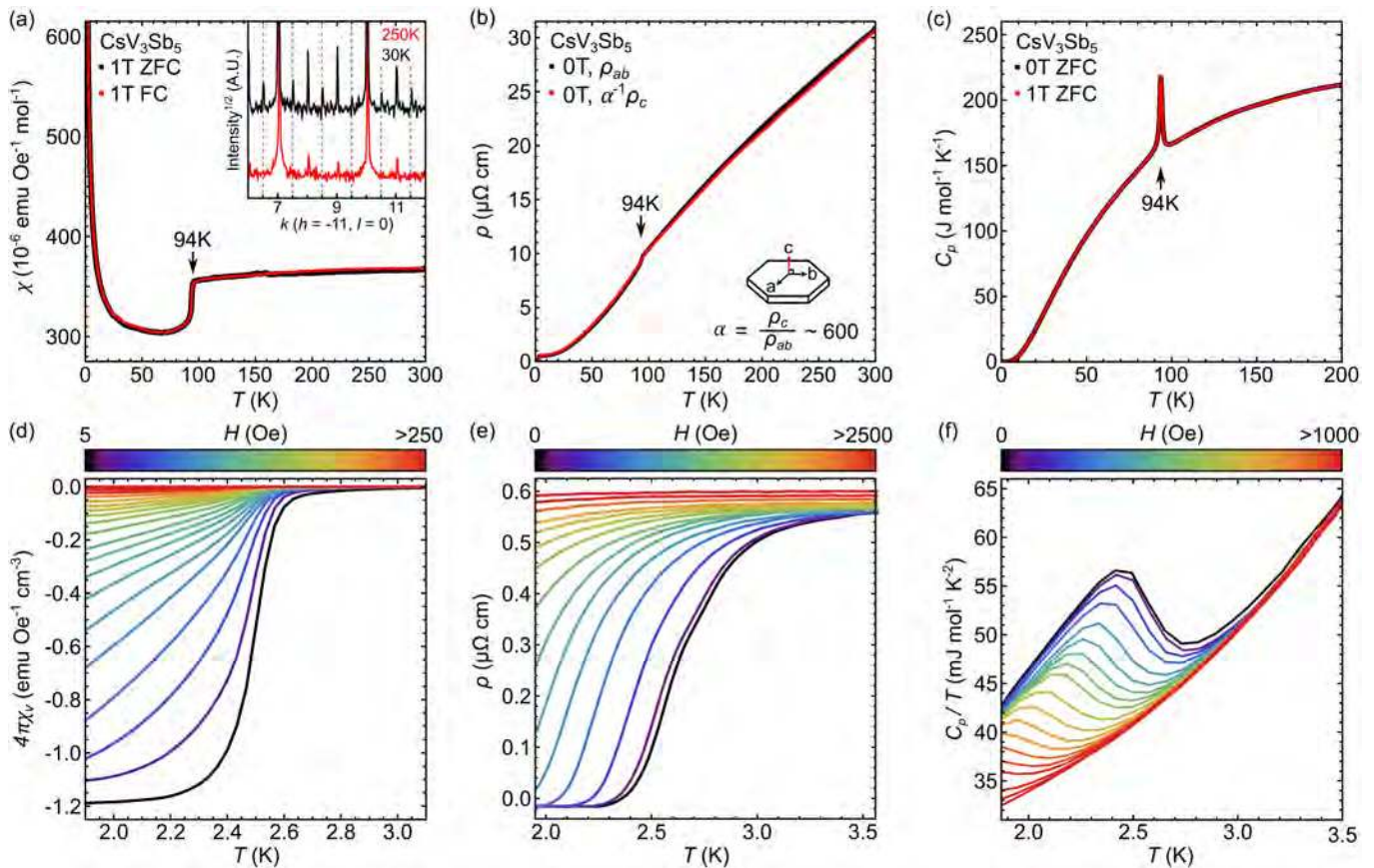
FIG. 2. (a,c,e) Full temperature ranges for the magnetization, electrical resistivity, and heat capacity, respectively, shown for single crystals of CsV_3Sb_5. All measurements indicate presence of an anomaly T^* at 94 K, suspected to be an electronic instability (e.g. charge ordering). The inset in panel (a) shows linecuts through x-ray diffraction data below and above T^*. Dashed lines denote the appearance of half-integer reflections (b, d, f) Field-dependent measurements at low temperatures, showing onset of superconductivity in magnetization, resistivity, and heat capacity, respectively. The T_c for CsV_3Sb_5 is approximately 2.5 K, with a slight suppression in resistivity due to high probe currents.

ure 3(a) shows both ARPES and DFT modeling data with the hexagonal Brillouin zone superimposed on the $E = 0$ eV constant energy contour and high symmetry points K, M, and Γ labeled. Data collected with differing photon energies did not reveal any appreciable dispersion along k_z, consistent with a quasi-2D band structure. ARPES data were collected at 50 K, 80 K, 100 K, and 120 K, and no resolvable changes were observed in the band structure when transitioning through the T^* transition. The DFT model shows remarkable agreement with the ARPES data, recovering all experimental observed crossings below the Fermi level. Figure 3(b) shows both the measured and calculated electronic structure hosts multiple Dirac points at finite binding energies.

While inaccessible in the present ARPES data, the DFT model further reveals multiple topological band features slightly above the Fermi energy. The $\overline{M}$-point is of particular interest, as M is a time-reversal invariant momentum (TRIM) point. Figure 4 shows the results of a tight binding calculation of surface states in CsV_3Sb_5,

where bright spots slightly above the Fermi energy indicate surface states.

Unlike many heavily studied kagome lattices (e.g. $ZnCu_3(OH)_6Cl_2$,[26–28] Fe_3Sn_2,[9, 29] Mn_3Ge,[30, 31] $Co_3Sn_2S_2$[10, 32, 33]), CsV_3Sb_5 does not exhibit resolvable magnetic order. Given that CsV_3Sb_5 possesses both time-reversal and inversion symmetry as well as a continuous, symmetry-enforced, direct gap at every k-point, one can calculate the $\mathbb{Z}_2$ topological invariant between each pair of bands near the Fermi level by simply analyzing the parity of the wave function at the TRIM (time-reversal invariant momentum) points [34]. This analysis reveals a number of topologically nontrivial crossings between adjacent bands in the region ± 1 eV from the Fermi level. For clarity, we will focus on the surface states crossing at the $\overline{M}$-point here with further analysis presented in the supplemental material [18]. Fig. 4(b) presents a close-up of the calculated surface states near the $\overline{M}$ point. The surface states at the $\overline{M}$-point manifest approximately 0.05 eV above the Fermi energy. The appar-
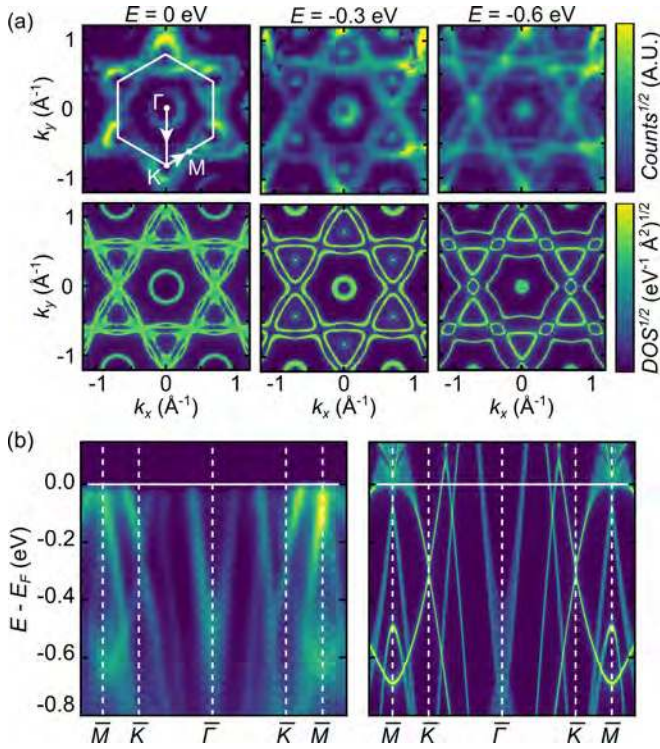
FIG. 3. Experimental ARPES data and comparison with DFT calculations. (a) A selection of constant energy maps at 80 K are compared with DFT calculations, showing excellent agreement. The hexagonal Brillouin zone is superimposed on the $E = 0$ eV data. (b) ARPES and DFT data tracing from M-K-Γ-K-M reveal multiple Dirac points throughout the dispersion. Surface states can be observed in the DFT data at the M-point, slightly above E_F.
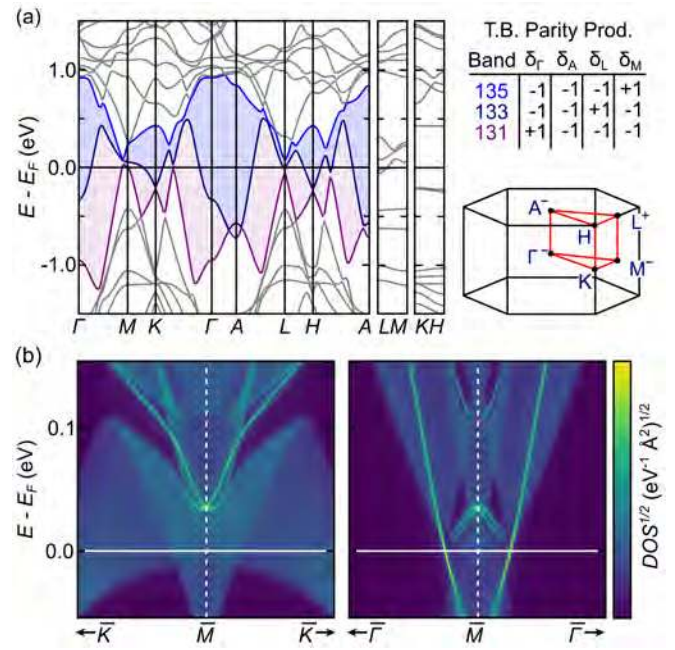

FIG. 4. (a) Calculated band structure of CsV_3Sb_5 along high symmetry directions across the Brillouin zone. A continuous direct gap (shaded) is noted and high symmetry points in the BZ are labeled. (b) Tight-binding model of CsV_3Sb_5 showing topologically-protected surfaces states that manifest at the time-reversal invariant momentum $\overline{M}$-point.

ent anisotropy in the calculated surface state dispersions ($\overline{M}$-$\overline{K}$ versus $\overline{M}$-$\overline{\Gamma}$) derives from the direct "gap" moving up or down in energy depending on direction away from the $\overline{M}$ point. This is not uncommon amongst topological metals [35–37].

Topologically nontrivial surface states close to E_F and the continuous direct gap throughout the Brillouin zone allow the identification of the normal state as a $\mathbb{Z}_2$ topological metal [38, 39]. The T^* transition in this compound also suggests that electronic interactions are appreciable in this material. This transition is accompanied by a subtle change in the derivative of the lattice parameters, cell volume, and associated crystallographic parameters upon crossing T^* [18]. Single crystal x-ray diffraction further shows the formation of a weak superlattice of charge scattering at half-integer reflections (an example shown in the inset of Fig. 2 (a)) [18].

The presence of a weak, structural superlattice is suggestive of a secondary structural response to a primary electronic order parameter such as a charge or bond density wave instability. Theoretical studies of partially filled kagome lattices predict a wide array of electronic order parameters [11]. The metallic nature of CsV_3Sb_5 and its

high degree of covalency makes formal charge assignment imprecise; however, in the ionic limit, the kagome lattice of V-sites would possess one electron per triangle (1/6 filling). Charge density wave (CDW) order with a (π, 0) in-plane wave vector consistent with our single crystal x-ray diffraction data is predicted in spinful models and spinless fermion models of interacting electrons in a partially filled kagome lattice.[11]

Nesting across a two-dimensional Fermi surface with an underlying hexagonal motif is also thought to promote the formation of a superconducting state [14]. Competing density wave instabilities may also arise, and in the present case, scattering along the (π, 0) wave vector would connect an enhanced density of states at saddle points near the Fermi energy at the M-points in CsV_3Sb_5's band structure. To our knowledge, this is the first material example hosting the band structure, Fermi energy, and ground state requisite for this theoretical mechanism. Given the CDW-like instability observed at T^* in this compound, interactions along this wave vector are likely enhanced and may promote a competition between CDW and superconducting instabilities. Although a structural superlattice exists, ARPES data do not resolve spectral broadening of the Fermi surface across the nested M-points, consistent with the long-range, weak nature of the high temperature density wave order. Unconventional superconductivity with chiral d-wave pair-

ing may emerge in this scenario [1, 13].

Superconductivity manifest within an electronically two-dimensional kagome lattice is rare unto itself. While other materials with kagome networks embedded within their lattice structures are known to superconduct (e.g. in certain silicides and borides [40, 41]), all of these examples are inherently three-dimensional both structurally and electronically. CsV_3Sb_5 seemingly opens a unique opportunity for mapping to models of nesting-driven instabilities emergent within a two-dimensional kagome metal. Isostructural variants KV_3Sb_5 and RbV_3Sb_5 host similar T^* transitions at 80 K and 104 K respectively, likely indicative of a similar high-temperature density wave order [16]; however superconductivity has only been observed in CsV_3Sb_5 to date. Understanding the interplay between the potentially competing T^* order parameter and the formation of superconductivity across the AV_3Sb_5 family is an interesting topic for future study.

The $\mathbb{Z}_2$ topological band structure of CsV_3Sb_5 may also be of interest for stabilizing the formation of Majorana modes within the vortex cores of a natively proximitized, superconducting surface state. Materials hosting both topologically nontrivial surface states and a native superconducting ground state are uncommon, with relatively few promising candidates identified in $FeSe_{(1-x)}Te_x$,[42–46] doped-Bi_2Se_3,[47–51] and $Sn_{(1-x)}In_xTe$[52–54]. With relatively light electron-doping (such as Ba substitution), CsV_3Sb_5 can likely be driven into a regime where such a proximitized topological surface state could be tested.

In summary, our results demonstrate that kagome metals can serve as a rich arena for exploring the interplay between correlated electron effects and superconductivity within a topologically nontrivial band structure. Our results demonstrate bulk superconductivity with $T_c = 2.5$ K in single crystals of CsV_3Sb_5 and classify its normal state as a $\mathbb{Z}_2$ topological metal with multiple topologically nontrivial band crossings in close proximity to the Fermi level. An anomalous CDW-like transition in the normal state suggests strong correlation effects and an electronic instability that weakly couples to the lattice. Future studies exploring the relation between this instability and the potential emergence of nesting-driven, unconventional superconductivity on the kagome lattice is motivated by our present results.

ACKNOWLEDGMENTS

---

* ortiz.brendenr@gmail.com
† stephendwilson@ucsb.edu
[1] W.-S. Wang, Z.-Z. Li, Y.-Y. Xiang, and Q.-H. Wang, Phys. Rev. B **87**, 115135 (2013).
[2] S. V. Isakov, S. Wessel, R. G. Melko, K. Sengupta, and Y. B. Kim, Phys. Rev. Lett. **97**, 147202 (2006).
[3] A. O'Brien, F. Pollmann, and P. Fulde, Phys. Rev. B **81**, 235115 (2010).
[4] A. Rüegg and G. A. Fiete, Phys. Rev. B **83**, 165118 (2011).
[5] S. Yan, D. A. Huse, and S. R. White, Science **332**, 1173 (2011).
[6] H.-M. Guo and M. Franz, Phys. Rev. B **80**, 113102 (2009).
[7] W.-H. Ko, P. A. Lee, and X.-G. Wen, Phys. Rev. B **79**, 214502 (2009).
[8] M. Kang, L. Ye, S. Fang, J.-S. You, A. Levitan, M. Han, J. I. Facio, C. Jozwiak, A. Bostwick, E. Rotenberg, *et al.*, Nat. Mater. **19**, 163 (2020).
[9] L. Ye, M. Kang, J. Liu, F. Von Cube, C. R. Wicker, T. Suzuki, C. Jozwiak, A. Bostwick, E. Rotenberg, D. C. Bell, *et al.*, Nature **555**, 638 (2018).
[10] N. Morali, R. Batabyal, P. K. Nag, E. Liu, Q. Xu, Y. Sun, B. Yan, C. Felser, N. Avraham, and H. Beidenkopf, Science **365**, 1286 (2019).
[11] J. Wen, A. Rüegg, C.-C. J. Wang, and G. A. Fiete, Phys. Rev. B **82**, 075125 (2010).
[12] S.-L. Yu and J.-X. Li, Phys. Rev. B **85**, 144402 (2012).
[13] R. Nandkishore and A. V. Chubukov, Phys. Rev. B **86**, 115426 (2012).
[14] R. Nandkishore, L. Levitov, and A. Chubukov, Nature Physics **8**, 158 (2012).
[15] M. L. Kiesel, C. Platt, and R. Thomale, Phys. Rev. Lett. **110**, 126405 (2013).
[16] B. R. Ortiz, L. C. Gomes, J. R. Morey, M. Winiarski, M. Bordelon, J. S. Mangum, I. W. Oswald, J. A. Rodriguez-Rivera, J. R. Neilson, S. D. Wilson, *et al.*, Phys. Rev. Mater. **3**, 094407 (2019).

[17] S.-Y. Yang, Y. Wang, B. R. Ortiz, D. Liu, J. Gayles, E. Derunova, R. Gonzalez-Hernandez, L. Smejkal, Y. Chen, S. S. Parkin, *et al.*, Sci. Adv. **6** (2020).

[18] See Supplemental material for experimental and theoretical details and supporting results, which includes Refs.[20, 55–68].

[19] A. A. Coelho, J. Appl. Crystallogr. **51**, 210 (2018).

[20] K. Momma and F. Izumi, J. Appl. Crystallogr. **44**, 1272 (2011).

[21] G. Kresse and J. Hafner, Phys. Rev. B **49**, 14251 (1994).

[22] G. Kresse and J. Furthmüller, Phys. Rev. B **54**, 11169 (1996).

[23] G. Kresse and J. Furthmüller, Comput. Mater. Sci. **6**, 15 (1996).

[24] P. E. Blöchl, Phys. Rev. B **50**, 17953 (1994).

[25] G. Kresse and D. Joubert, Phys. Rev. B **59**, 1758 (1999).

[26] R. Braithwaite, K. Mereiter, W. Paar, and A. Clark, Mineral. Mag. **68**, 527 (2004).

[27] D. E. Freedman, T. H. Han, A. Prodi, P. Müller, Q.-Z. Huang, Y.-S. Chen, S. M. Webb, Y. S. Lee, T. M. McQueen, and D. G. Nocera, J. Am. Chem. Soc. **132**, 16185 (2010).

[28] T.-H. Han, J. S. Helton, S. Chu, D. G. Nocera, J. A. Rodriguez-Rivera, C. Broholm, and Y. S. Lee, Nature **492**, 406 (2012).

[29] Q. Wang, Q. Yin, and H. Lei, Chin. Phys. B **29**, 017101 (2020).

[30] A. K. Nayak, J. E. Fischer, Y. Sun, B. Yan, J. Karel, A. C. Komarek, C. Shekhar, N. Kumar, W. Schnelle, J. Kübler, *et al.*, Sci. Adv. **2**, e1501870 (2016).

[31] N. Kiyohara, T. Tomita, and S. Nakatsuji, Phys. Rev. Appl. **5**, 064009 (2016).

[32] P. Vaqueiro and G. G. Sobany, Solid State Sci. **11**, 513 (2009).

[33] Q. Xu, E. Liu, W. Shi, L. Muechler, J. Gayles, C. Felser, and Y. Sun, Phys. Rev. B **97**, 235416 (2018).

[34] L. Fu and C. L. Kane, Phys. Rev. B **76**, 045302 (2007).

[35] B. Singh, X. Zhou, H. Lin, and A. Bansil, Phys. Rev. B **97**, 075125 (2018).

[36] I. Cucchi, A. Marrazzo, E. Cappelli, S. Riccò, F. Y. Bruno, S. Lisi, M. Hoesch, T. K. Kim, C. Cacho, C. Besnard, E. Giannini, N. Marzari, M. Gibertini, F. Baumberger, and A. Tamai, Phys. Rev. Lett. **124**, 106402 (2020).

[37] R. Yu, H. Weng, Z. Fang, X. Dai, and X. Hu, Phys. Rev. Lett. **115**, 036807 (2015).

[38] L. M. Schoop, L. S. Xie, R. Chen, Q. D. Gibson, S. H. Lapidus, I. Kimchi, M. Hirschberger, N. Haldolaarachchige, M. N. Ali, C. A. Belvin, *et al.*, Phys. Rev. B **91**, 214517 (2015).

[39] J. Nayak, S.-C. Wu, N. Kumar, C. Shekhar, S. Singh, J. Fink, E. E. Rienks, G. H. Fecher, S. S. Parkin, B. Yan, *et al.*, Nat. Commun. **8**, 13942 (2017).

[40] U. Rauchschwalbe, W. Lieke, F. Steglich, C. Godart, L. Gupta, and R. Parks, Phys. Rev. B **30**, 444 (1984).

[41] H.-Y. Lu, N.-N. Wang, L. Geng, S. Chen, Y. Yang, W.-J. Lu, W.-S. Wang, and J. Sun, Europhys. Lett. **110**, 17003 (2015).

[42] Z. Wang, P. Zhang, G. Xu, L. Zeng, H. Miao, X. Xu, T. Qian, H. Weng, P. Richard, A. Fedorov, *et al.*, Phys. Rev. B **92**, 115119 (2015).

[43] G. Xu, B. Lian, P. Tang, X.-L. Qi, and S.-C. Zhang, Phys. Rev. Lett. **117**, 047001 (2016).

[44] X. Wu, S. Qin, Y. Liang, H. Fan, and J. Hu, Phys. Rev. B **93**, 115129 (2016).

[45] P. Zhang, K. Yaji, T. Hashimoto, Y. Ota, T. Kondo, K. Okazaki, Z. Wang, J. Wen, G. Gu, H. Ding, *et al.*, Science **360**, 182 (2018).

[46] T. Machida, Y. Sun, S. Pyon, S. Takeda, Y. Kohsaka, T. Hanaguri, T. Sasagawa, and T. Tamegai, Nat. Mater. , 1 (2019).

[47] L. Fu and E. Berg, Phys. Rev. Lett. **105**, 097001 (2010).

[48] M. Kriener, K. Segawa, Z. Ren, S. Sasaki, and Y. Ando, Phys. Rev. Lett. **106**, 127004 (2011).

[49] S. Sasaki, M. Kriener, K. Segawa, K. Yada, Y. Tanaka, M. Sato, and Y. Ando, Phys. Rev. Lett. **107**, 217001 (2011).

[50] Z. Liu, X. Yao, J. Shao, M. Zuo, L. Pi, S. Tan, C. Zhang, and Y. Zhang, J. Am. Chem. Soc. **137**, 10512 (2015).

[51] G. Du, Y. Li, J. Schneeloch, R. Zhong, G. Gu, H. Yang, H. Lin, and H.-H. Wen, Sci. China. Phys. Mech. **60**, 037411 (2017).

[52] T. Sato, Y. Tanaka, K. Nakayama, S. Souma, T. Takahashi, S. Sasaki, Z. Ren, A. Taskin, K. Segawa, and Y. Ando, Phys. Rev. Lett. **110**, 206804 (2013).

[53] M. Novak, S. Sasaki, M. Kriener, K. Segawa, and Y. Ando, Phys. Rev. B **88**, 140502 (2013).

[54] C. Polley, V. Jovic, T.-Y. Su, M. Saghir, D. Newby Jr, B. Kowalski, R. Jakiela, A. Barcz, M. Guziewicz, T. Balasubramanian, *et al.*, Phys. Rev. B **93**, 075132 (2016).

[55] J. Sangster and A. Pelton, J. Phase Equilibria **18**, 382 (1997).

[56] A. Hammersley, S. Svensson, M. Hanfland, A. Fitch, and D. Hausermann, High Press. Res. **14**, 235 (1996).

[57] S. P. Westrip, J. Appl. Crystallogr. **43**, 920 (2010).

[58] G. Jennings, "Crystal coordinate transformation workflow (CCTW)," Software available at https://sourceforge.net/projects/cctw/.

[59] R. Osborn and J. Wozniak, "NexPy," Software available at https:github.com/nexpy/nexpy.

[60] J. Sun, A. Ruzsinszky, and J. P. Perdew, Phys. Rev. Lett. **115**, 036402 (2015).

[61] S. Grimme, J. Comput. Chem. **27**, 1787 (2006).

[62] S. Grimme, S. Ehrlich, and L. Goerigk, J. Comput. Chem. **32**, 1456 (2011).

[63] J. P. Perdew, K. Burke, and M. Ernzerhof, Phys. Rev. Lett. **77**, 3865 (1996).

[64] A. A. Mostofi, J. R. Yates, G. Pizzi, Y.-S. Lee, I. Souza, D. Vanderbilt, and N. Marzari, Comput. Phys. Commun. **185**, 2309 (2014).

[65] M. P. L. Sancho, J. M. L. Sancho, and J. Rubio, J. Phys. F **15**, 851 (1985).

[66] Q.-S. Wu, S.-N. Zhang, H.-F. Song, M. Troyer, and A. A. Soluyanov, Comput. Phys. Commun. **224**, 405 (2018).

[67] J. Gao, Q. Wu, C. Persson, and Z. Wang, arXiv preprint arXiv:2002.04032 (2020).

[68] G. F. Koster, *Properties of the thirty-two point groups*, Vol. 24 (The MIT Press, 1963).

CsV$_3$Sb$_5$: a $\mathbb{Z}_2$ topological kagome metal with a superconducting ground state

Brenden R. Ortiz,[1, *] Samuel M.L. Teicher,[1] Yong Hu,[2] Julia L. Zuo,[1] Paul M. Sarte,[1] Emily
C. Schueller,[1] A.M. Milinda Abeykoon,[3] Matthew J. Krogstad,[4] Stephan Rosenkranz,[4]
Raymond Osborn,[4] Ram Seshadri,[1] Leon Balents,[5] Junfeng He,[2] and Stephen D. Wilson[1, †]

[1]*Materials Department and California Nanosystems Institute,*
University of California Santa Barbara, Santa Barbara, CA, 93106, United States
[2]*University of Science and Technology of China, Hefei, Anhui, 230026, China*
[3]*National Synchrotron Light Source II, Brookhaven National Laboratory, Upton, New York 11973, USA*
[4]*Materials Science Division, Argonne National Laboratory, Lemont, Illinois 60439-4845, USA*
[5]*Kavli Institute for Theoretical Physics, University of California,*
Santa Barbara, Santa Barbara, California 93106, USA
(Dated: November 15, 2020)

METHODS

Crystal and powder synthesis

Single crystals and powders of CsV$_3$Sb$_5$ were synthesized from Cs (liquid, Alfa 99.98%), V (powder, Sigma 99.9%) and Sb (shot, Alfa 99.999%). As-received vanadium powder was purified in-house to remove residual oxides. Due to extreme reactivity of elemental Cs, all further preparation of CsV$_3$Sb$_5$ was performed in an argon glovebox with oxygen and moisture levels <0.5 ppm. Single crystals of CsV$_3$Sb$_5$ were synthesized using the self-flux method. The flux is a eutectic mixture of CsSb Cs$_3$Sb$_7$[1] mixed with VSb$_2$. Elemental reagents were milled in a pre-seasoned tungsten carbide vial to form a composition which is 50 at.% Cs$_x$Sb$_y$ eutectic and approximately 50 at.% VSb$_2$. The fluxes were loaded into alumina crucibles and sealed within stainless steel jackets. The samples were heated to 1000°C at 250°C/hr and soaked there for 24 h. The samples were subsequently cooled to 800°C at 100°C/hr and then further to 500°C at 2°C/hr. Once cooled, the excess flux is removed using water to etch away the Cs$_x$Sb$_y$ phases.

To circumvent high reactivity of elemental Cs, powders were synthesized by mechanochemical methods. Elemental reagents were added to a tungsten carbide ball mill vial with Cs in slight excess (Cs$_{1.05}$V$_3$Sb$_5$). Powder was ball-milled for 1 h in a Spex 8000M high-energy ball mill. To avoid contamination, the tungsten carbide vial was pre-seasoned and cleaned with Sb between runs. Powders were subsequently ground in an agate mortar, sieved through a 100 micron mesh, and annealed for 150 h at 550°C. For transport measurements, powders were consolidated using a 1 ton uniaxial press. Resulting pellets were annealed at 450°C for 24 h under static vacuum. A sacrificial layer of powder was lightly packed around the pellets to prevent Cs loss during the vacuum anneal.

Bulk electronic properties measurements

Magnetization measurements were performed using a Quantum Design Squid Magnetometer (MPMS3) in vibrating-sample measurement mode (VSM). Compacted, annealed polycrystalline pellets were sliced into rectangular prisms with 2 mm width, 2 mm length, and 1 mm height. The pellet was attached to a Quantum Design quartz MPMS paddle using GE varnish. To minimize demagnetization effects, the pellet was mounted with the square face perpendicular to the field. Single crystals were attached to quartz paddles using GE varnish as well. As the crystals are plate-like, mounting with the c-axis perpendicular to the field also minimizes demagnetization effects.

Resistivity measurements were performed using a Quantum Design Dynacool Physical Properties Measurement System (PPMS). For resistivity, polycrystalline pellets were sliced into rectangular prisms with approximately 1 mm width, 4 mm length, and 1 mm height. Electrical contacts were made in the standard 4-point geometry using gold wire and silver paint. Thermal contact and electrical isolation was ensured using layers of GE varnish and cigarette paper, as recommended by Quantum Design. Resistivity measurements on polycrystalline samples were performed with a 1 mA current. Single crystal measurements were performed in an analogous fashion, with typical sample sizes of 1 mm width, 2 mm length, and 0.1 mm thickness. Samples were mounted such that the c-axis was parallel to the field (flat plates mounted flush on resistivity stage). Due to low resistivity, single crystal measurements must be performed with an increased current of 8 mA current.

Heat capacity measurements were performed on a Quantum Design Dynacool PPMS. Polycrystalline pellets were sliced into small rectangular prisms with approximately 1 mm width, 1 mm length, and 0,5 mm height. Apezion N grease was used to ensure thermal and mechanical contact with heat capacity stage. Sample coupling returned by the instrument was consistently >95%. Single crystal measurements were performed in

an analogous fashion, with crystals mounted such that the c-axis was parallel to the field (flat plates mounted flush on heat capacity stage).

Scattering measurements

The phase purities of powders were confirmed through laboratory X-ray diffraction using a Panalytical Empyrean diffractometer with Cukα radiation at room temperature. Temperature-dependent X-ray powder diffraction data was collected at Brookhaven National Laboratory (beamline 28-ID-1) with $\lambda = 0.1671\,\text{Å}$ radiation in a capillary transmission geometry using a PerkinElmer amorphous silicon area detector. Powders were sealed in Kapton capillaries. Two dimensional diffraction data were integrated using Fit2D software package [2]. Rietveld refinements of temperature-dependent diffraction were performed using TOPAS Academic V6. Single crystal structures were verified through the publCIF program [3]. Structure visualization was performed with the VESTA software package [4].

Volumes of diffuse X-ray scattering data were measured from single crystals at Sector 6-ID-D at the Advanced Photon Source using high energy x-rays with an incident energy of $87.1\,\text{keV}$ and a Dectris 2M Pilatus CdTe detector by continuously rotating the sample at $1°$ per second over $370°$ while reading out images at $10\,\text{Hz}$ frequency. Data were collected from $30\,\text{K}$ to $300\,\text{K}$, with samples cooled by flowing He gas below $100\,\text{K}$ and N_2 gas above $100\,\text{K}$. Three sets of rotation images were collected for each sample at each temperature to fill in gaps between the detector chips. The resulting images were stacked into a three-dimensional array, oriented using an automated peak search algorithm and transformed in reciprocal space coordinates using the software package CCTW (Crystal Coordinate Transformation Workflow) [5] and further analyzed using the NeXpy package [6].

ARPES measurements

Angle-resolved photoemission measurements (ARPES) were obtained at the Stanford Synchrotron Radiation Lightsource (SSRL, beamline 5-2), a division of the SLAC National Accelerator Laboratory. $120\,\text{eV}$ photons were used with an energy resolution of $20\,\text{meV}$. Exfoliated crystals of CsV_3Sb_5 were placed on copper posts under a vacuum of $<3\times10^{-11}\,\text{Torr}$. The Fermi level of CsV_3Sb_5 was obtained by measuring polycrystalline Au in electrical contact with the sample.

Computational details

In order to address potential orbital localization (particularly V d) and the van der Waals forces that play a role in c-layer stacking in this compound, we performed simulations using the SCAN functional [7] and D2/D3 [8, 9] dispersion corrections as well as the more standard PBE functional [10]. Calculations described in the text employed PBE with D3 corrections as this functional choice gave relaxed lattice parameters with excellent matching to the room temperature experimental values for CsV_3Sb_5 (see Table S8).

For comparison to ARPES data, we used Wannier90 [11] to fit Wannier functions and construct a tight-binding model starting from initial projectors corresponding to valence orbitals (Cs s, p; V s, p, d; Sb s, p; with a frozen fitting window $E_F \pm 2\,\text{eV}$). Surface Green's function calculations were calculated using the Sancho 1985 algorithm [12] as implemented in the Wannier Tools package [13]. Irrep assignments for the $\mathbb{Z}_2$ topological invariant calculation were performed using the IRVSP program in conjunction with VASP [14].

* ortiz.brendenr@gmail.com
† stephendwilson@ucsb.edu

[1] J. Sangster and A. Pelton, J. Phase Equilibria **18**, 382 (1997).
[2] A. Hammersley, S. Svensson, M. Hanfland, A. Fitch, and D. Hausermann, High Press. Res. **14**, 235 (1996).
[3] S. P. Westrip, J. Appl. Crystallogr. **43**, 920 (2010).
[4] K. Momma and F. Izumi, J. Appl. Crystallogr. **44**, 1272 (2011).
[5] G. Jennings, "Crystal coordinate transformation workflow (CCTW)," Software available at https://sourceforge.net/projects/cctw/.
[6] R. Osborn and J. Wozniak, "NexPy," Software available at https:github.com/nexpy/nexpy.
[7] J. Sun, A. Ruzsinszky, and J. P. Perdew, Phys. Rev. Lett. **115**, 036402 (2015).
[8] S. Grimme, J. Comput. Chem. **27**, 1787 (2006).
[9] S. Grimme, S. Ehrlich, and L. Goerigk, J. Comput. Chem. **32**, 1456 (2011).
[10] J. P. Perdew, K. Burke, and M. Ernzerhof, Phys. Rev. Lett. **77**, 3865 (1996).
[11] A. A. Mostofi, J. R. Yates, G. Pizzi, Y.-S. Lee, I. Souza, D. Vanderbilt, and N. Marzari, Comput. Phys. Commun. **185**, 2309 (2014).
[12] M. P. L. Sancho, J. M. L. Sancho, and J. Rubio, J. Phys. F **15**, 851 (1985).
[13] Q.-S. Wu, S.-N. Zhang, H.-F. Song, M. Troyer, and A. A. Soluyanov, Comput. Phys. Commun. **224**, 405 (2018).
[14] J. Gao, Q. Wu, C. Persson, and Z. Wang, arXiv preprint arXiv:2002.04032 (2020).
[15] G. F. Koster, *Properties of the thirty-two point groups*, Vol. 24 (The MIT Press, 1963).
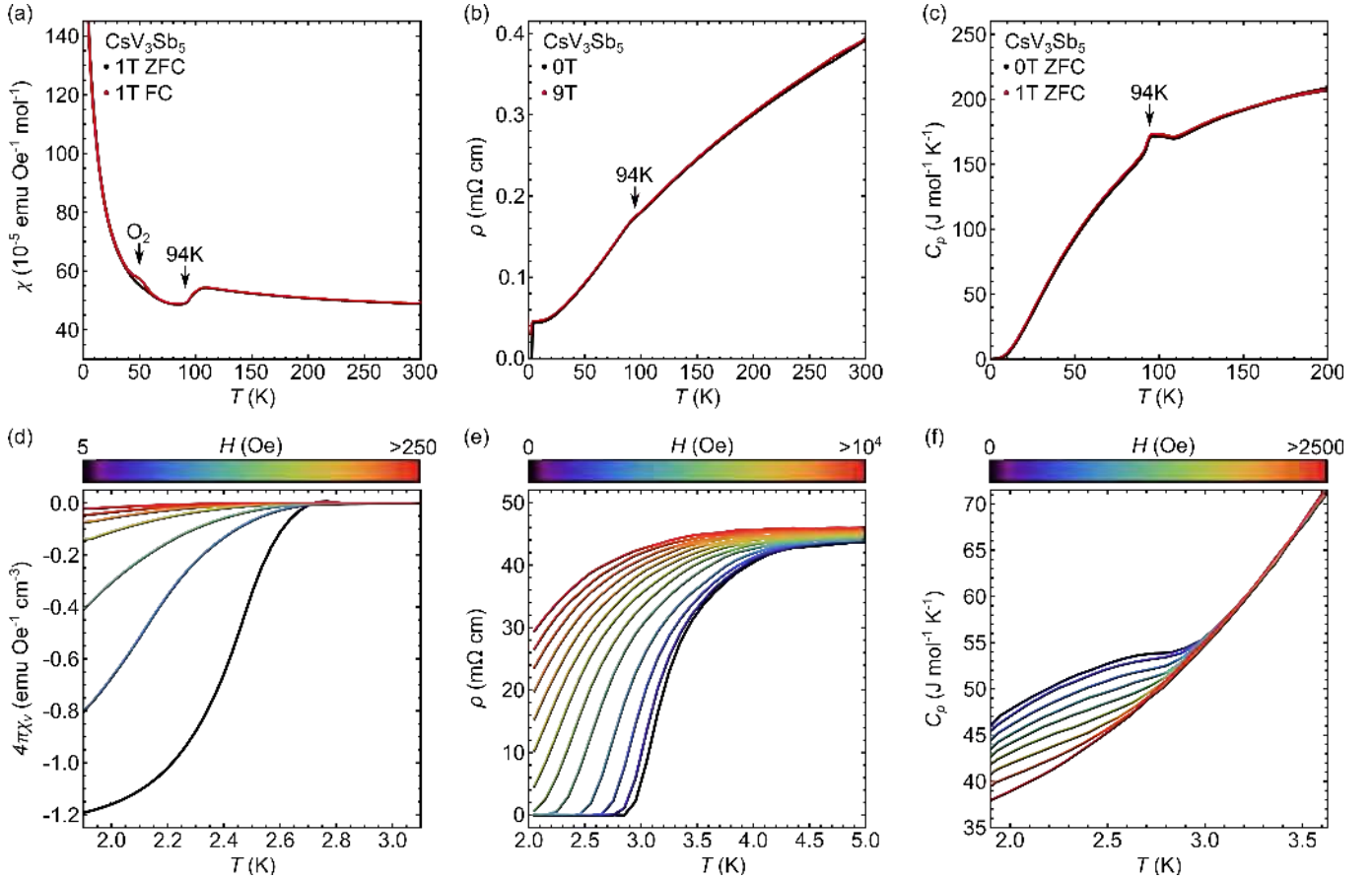
SFig 1. Transport measurements performed on sintered pellets of CsV_3Sb_5 powder, provided as comparison to single crystal work in main body (Figure 2). (a,b,c) Magnetization, resistivity, and heat capacity data collected over a broad range of temperatures, demonstrating the $T^* = 94\,K$ anomaly in powders. (d,e,f) Transport data collected at low temperatures showing bulk superconductivity, although transition is broad in powders relative to single crystals.
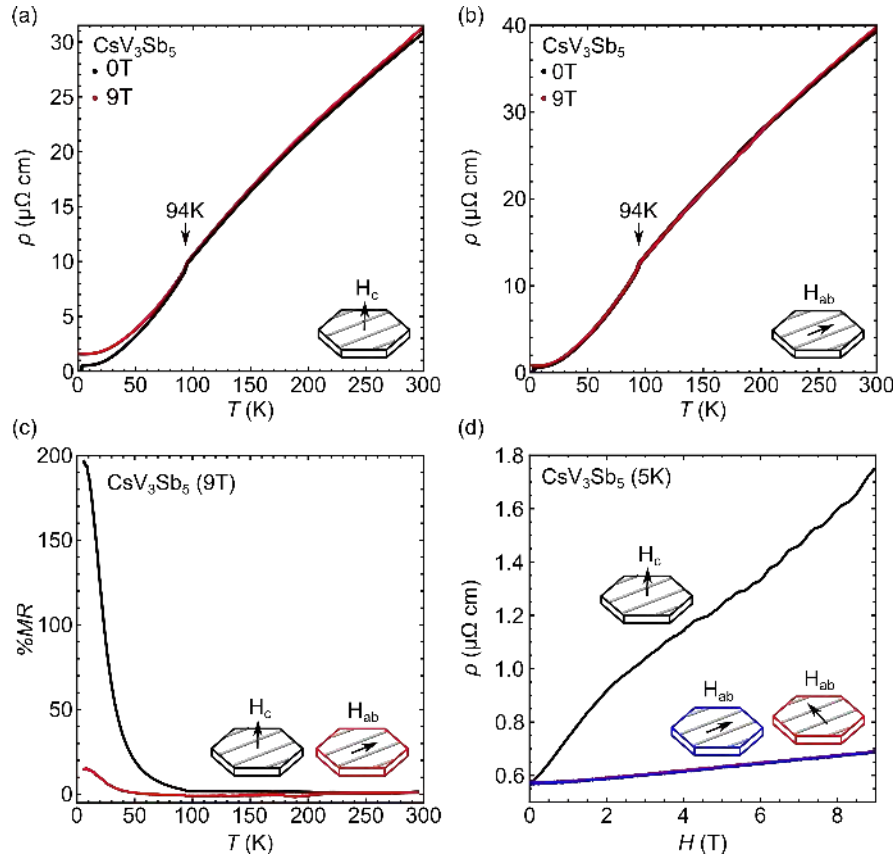
SFig 2. (a) Single crystal resistivity measurements performed with the magnetic field parallel to c-axis and current flowing in the ab-plane. (b) Resistivity measurements performed with magnetic field applied within the ab-plane and parallel to the current flow. (c) Magnetoresistance percentage comparing longitudinal and transverse transport measurements. (d) Resistivity versus field collected for three configurations: The black line denotes the current flowing in the ab-plane and the field applied along the c-axis, the red line denotes the current flowing in the ab-plane and perpendicular to an in-plane applied field, and the blue line denotes the current flowing in the ab-plane and parallel to an in-plane applied field.
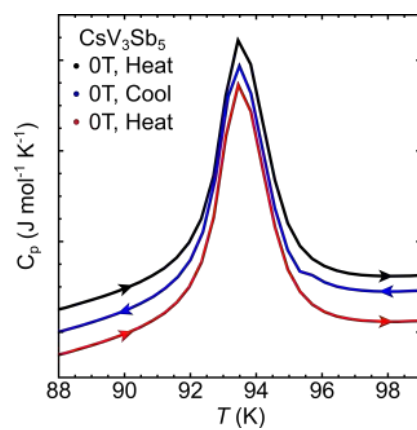
SFig 3. Heat capacity measurements collected on a single crystal of CsV_3Sb_5 across over multiple heating and cooling cycles. The heat capacity peak associated with the $T^* = 94\,\mathrm{K}$ transition is reliably reproduced in magnitude and position with no discernible hysteresis. Note that the curves have been manually offset in the y-direction for visual clarity.
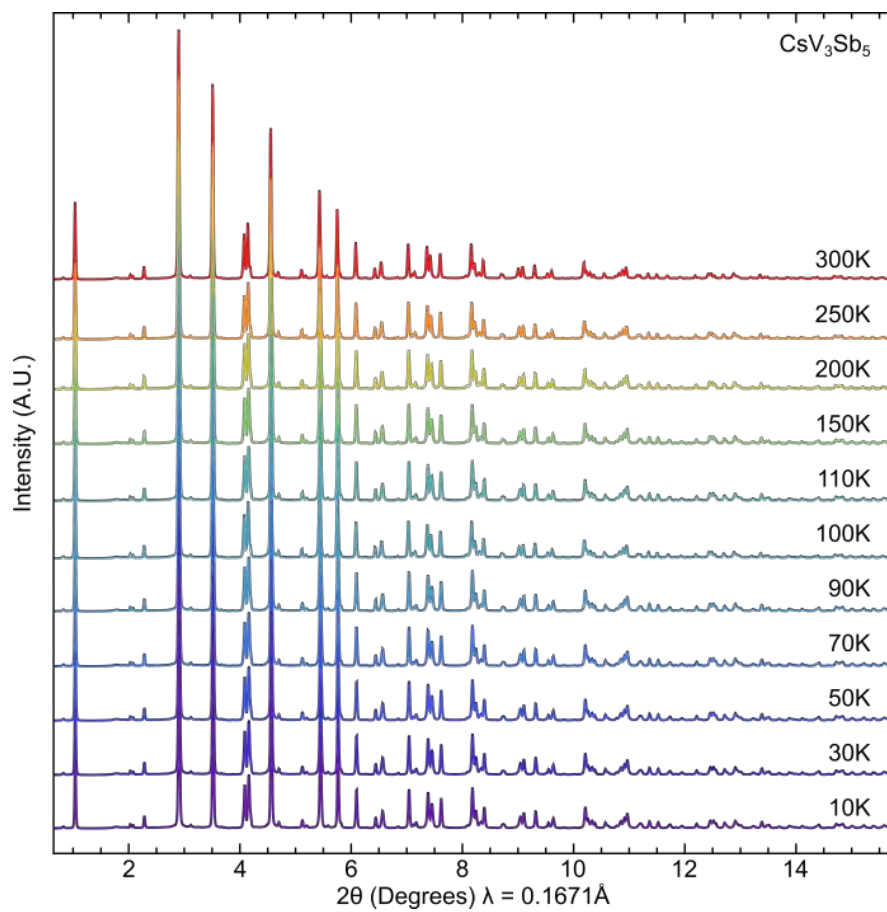
SFig 4. Temperature-dependent synchrotron powder diffraction on samples of CsV_3Sb_5. No structural transitions, extra peaks, or symmetry changes within resolution of the powder diffraction appear upon cooling through T^*. Data extracted from the Rietveld refinements is displayed in the supplementary figures, SFig. 5 and SFig. 6.
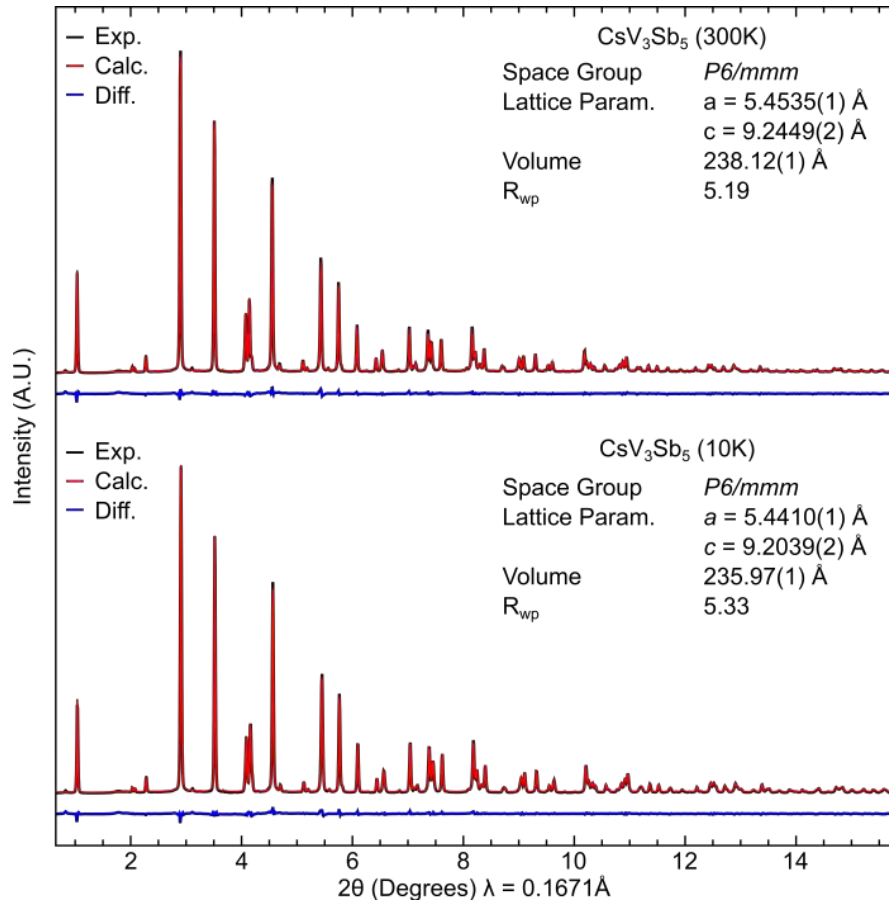
SFig 5. Fits generated from Rietveld refinements on CsV_3Sb_5 at temperatures well above (300K) and below (10K) the T^* anomaly (94K) observed in heat capacity, magnetization, and electrical resistivity. Within error, the low-temperature structure remains well described by the $P6/mmm$ space group.
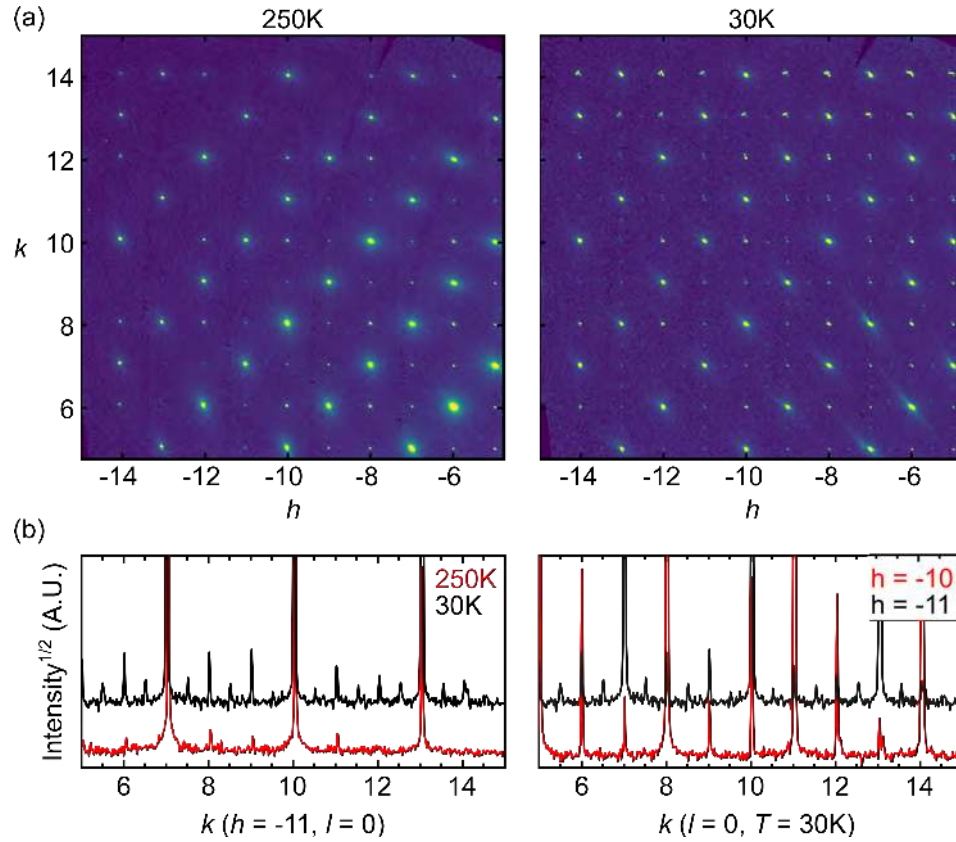
SFig 6. Synchrotron x-ray diffraction on single crystals of CsV_3Sb_5 reveal superlattice peaks upon cooling through the $T^* = 94$ K transition. (a) 2-D slices through Q-space showing the $(h, k, 0)$ diffraction plane at $T = 250$ K and $T = 30$ K. Faint superlattice peaks appear at half integer positions below the 94K transition. Note that the data is plotted on a rectangular grid. (b) Line cuts through $(h, k, 0)$ maps showing the appearance of superlattice peaks with decreasing temperature (left) and their dependence on the parity of h and k values (right). Diffraction data identifies superlattice peaks predominately appear at half-integer, odd, h/k values.
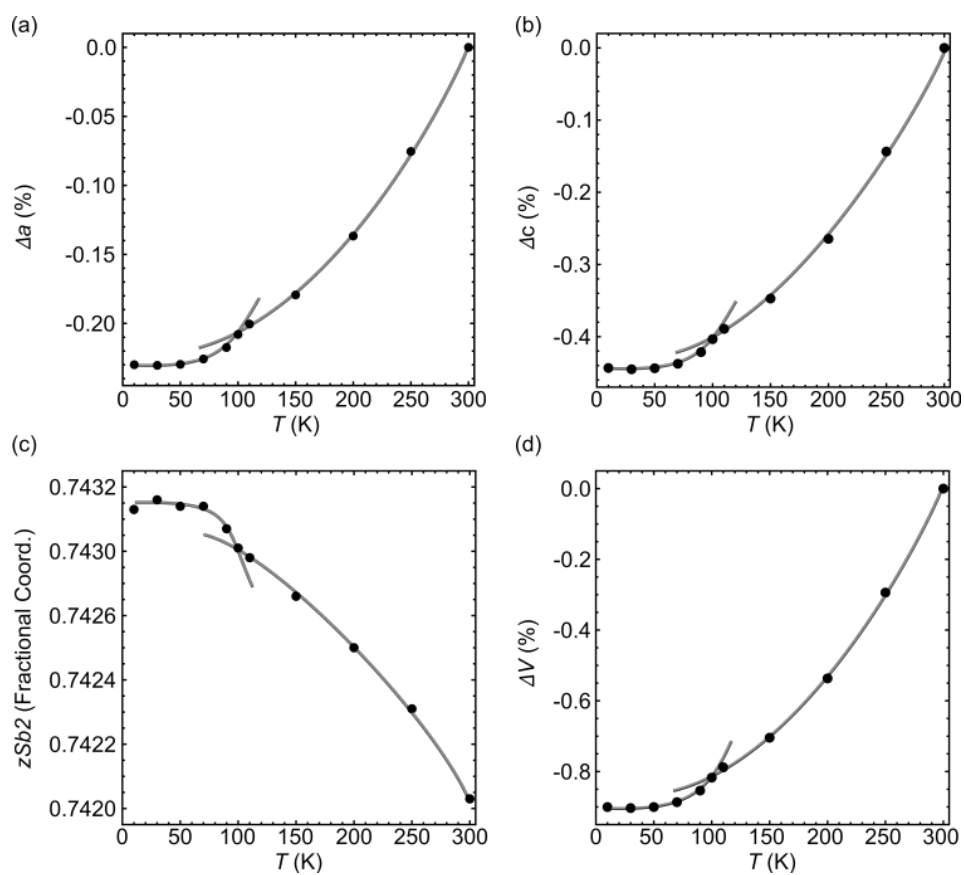
SFig 7. Although the $T^* = 94\,\mathrm{K}$ anomaly is subtle, clear structural changes appear in (a, b) the lattice parameters, (c) atomic positions, and (d) cell volume upon cooling through the transition. Gray lines act as guides to the eye to highlight the change near 94 K.

CsV$_3$Sb$_5$	a (Å)	% dev.	c (Å)	% dev.	c/a	% dev.
expt.	5.52	-	9.36	-	1.70	-
PBE	5.50	0.4%	9.87	5.5%	1.80	5.9%
PBE-D2.	5.51	0.2%	8.66	7.5%	1.57	7.7%
PBE-D3.	5.45	1.3%	9.35	0.1%	1.72	1.2%
SCAN	5.50	0.4%	9.64	3.0%	1.75	2.9%
SCAN-D2	5.44	1.5%	8.74	6.6%	1.61	5.3%
SCAN-D3	5.40	2.2%	9.16	2.1%	1.70	0.0%

SFig 8. Lattice parameter comparison between experiment and *ab intio* relaxed structures.
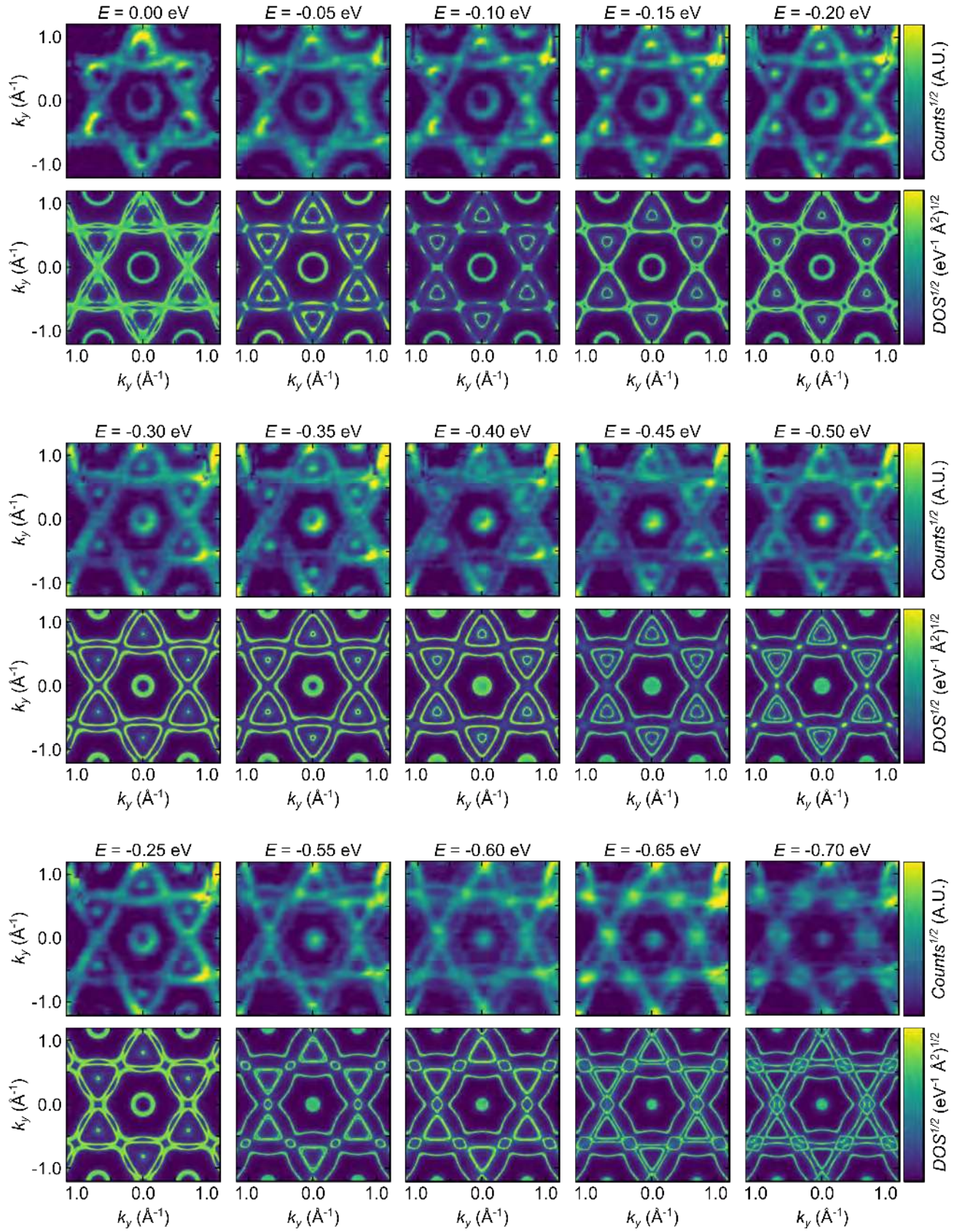
SFig 9. Additional angle-resolved photoemission spectroscopy (ARPES) data of CsV_3Sb_5 collected in increments of $0.05\,eV$ from the Fermi energy to $-0.7\,eV$. Excellent agreement is found between experimental data (top panels) and tight-binding models (bottom panels) over all energies.
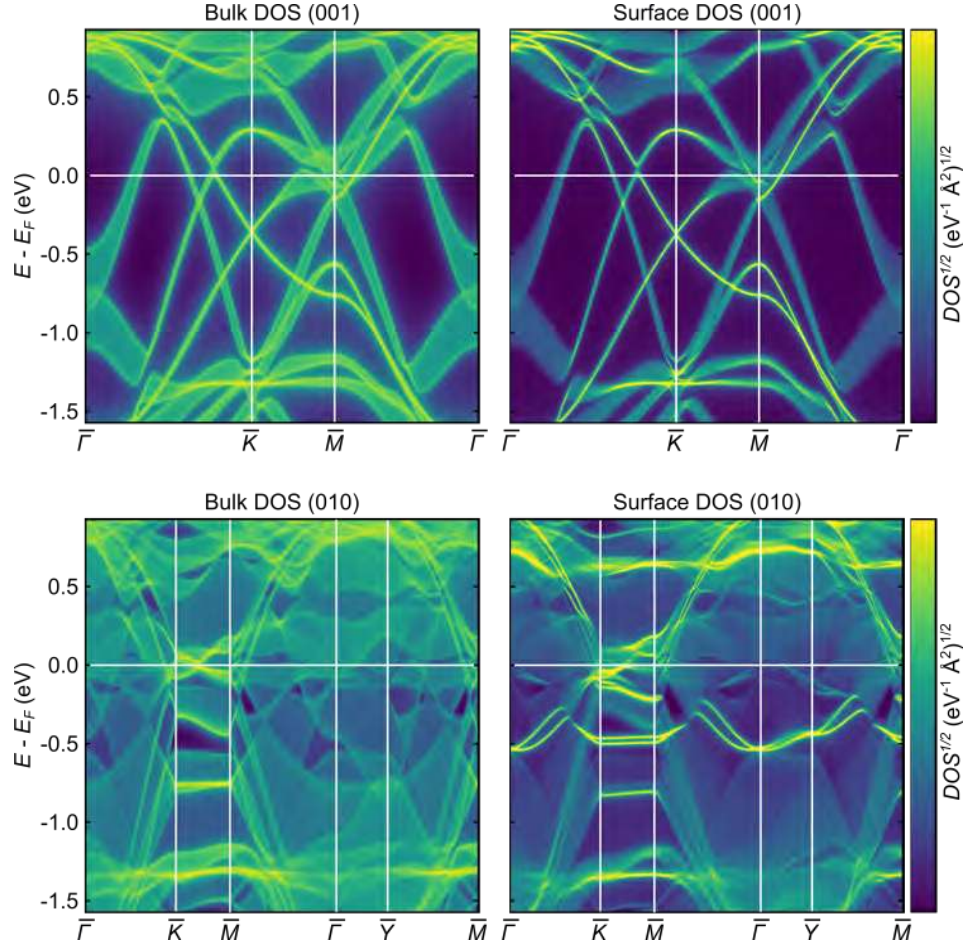
SFig 10. Tight-binding models were fit to DFT data, allowing a comparison of the bulk density of states and surface density of states on the (001) and (010) surfaces of CsV_3Sb_5. Comparing the bulk and surface DOS, a myriad of surface states can be seen throughout the electronic structure. The main body focuses on the time reversal invariant momentum (TRIM) point about $0.05\,eV$ above the Fermi energy, although there are many other candidate states below the Fermi energy as well.
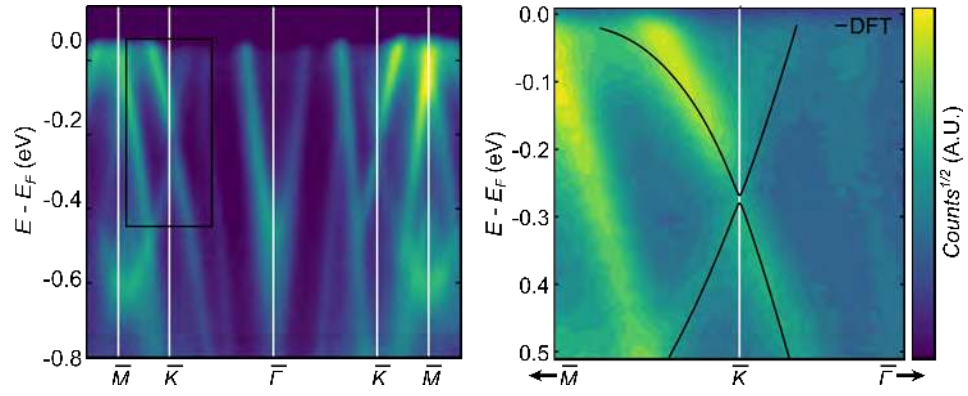
SFig 11. Experimental ARPES on single crystals of CsV_3Sb_5 reveals that the Dirac cone at K in CsV_3Sb_5 is slightly gapped.

band	irrep.				parity prod.				invar.
#	Γ	A	L	M	δ_Γ	δ_A	δ_L	δ_M	$\mathbb{Z}_2$
	$(D6h)$	$(D6h)$	$(D2h)$	$(D2h)$					
81	Γ_7^+	A_8^-	L_5^+	M_5^-	-1	1	-1	-1	-1
79	Γ_8^+	A_8^-	L_5^-	M_5^+	-1	-1	-1	1	-1
77	Γ_8^+	A_9^-	L_5^-	M_5^+	-1	1	1	1	-1
75	Γ_9^+	A_7^+	L_5^-	M_5^-	-1	-1	-1	1	-1
73	Γ_7^-	A_8^+	L_5^-	M_5^+	-1	-1	1	-1	-1
71	Γ_8^-	A_7^+	L_5^+	M_5^+	1	-1	-1	-1	-1
69	Γ_9^+	A_7^-	L_5^+	M_5^-	-1	-1	-1	-1	1
67	Γ_8^+	A_9^-	L_5^-	M_5^+	-1	1	-1	1	1
65	Γ_7^+	A_8^-	L_5^+	M_5^-	-1	-1	1	1	1
63	Γ_8^+	A_9^-	L_5^+	M_5^-	-1	1	1	-1	1
61	Γ_9^+	A_7^-	L_5^-	M_5^+	-1	-1	1	1	1
59	Γ_7^+	A_8^-	L_5^-	M_5^-	-1	1	-1	1	1
57	Γ_7^-	A_9^+	L_5^+	M_5^+	-1	-1	1	-1	-1
55	Γ_9^-	A_9^+	L_5^-	M_5^-	1	-1	1	-1	1
53	Γ_9^-	A_7^+	L_5^+	M_5^-	-1	-1	-1	1	-1
51	Γ_7^-	A_8^+	L_5^+	M_5^+	1	-1	-1	-1	-1
49	Γ_8^-	A_7^+	L_5^-	M_5^+	-1	-1	-1	-1	1
47	Γ_9^+	A_9^-	L_5^+	M_5^-	1	-1	1	-1	1
45	Γ_8^+	A_8^-	L_5^+	M_5^-	1	1	1	1	1
43	Γ_7^+	A_7^-	L_5^+	M_5^-	1	-1	1	-1	1

SFig 12. $\mathbb{Z}_2$ calculation for CsV$_3$Sb$_5$. Numbering of the irreducible representations (irreps) in the $D6h$ and $D2h$ point groups refers to the notation of Koster *et al* [15]. We use the band numbering scheme from the DFT simulation because this is a metal with no clear division between conduction and valence states. The topological surface states discussed in the body of the text occur between bands 133 and 135; such surface states are expected based on the $\mathbb{Z}_2 = -1$ topological classification for band 133. However, it can be seen that there are strong topological $\mathbb{Z}_2$ invariants for band gaps between all of the bands between 129 and 141, spanning an energy range of several eV. We therefore expect a range of near-Fermi level topological surface states may be chemically accessible in the material, for example through Fermi level lowering by ion de-intercalation.